

Article

Novel Alkali-Activated Materials with Photocatalytic and Bactericidal Properties Based on Ceramic Tile Waste

Ashley Bonilla, Mónica A. Villaquirán-Cacedo and Ruby Mejía de Gutiérrez * 

Composite Materials Group (CENM), School of Materials Engineering, Universidad del Valle, Cali 760032, Colombia; ashley.bonilla@correounivalle.edu.co (A.B.); monica.villaquiran@correounivalle.edu.co (M.A.V.-C.)

* Correspondence: ruby.mejia@correounivalle.edu.co

Abstract: Ceramics tile wastes (CWs) were mechanically conditioned for the preparation of alkali-activated hybrid-cements from CW (90 wt.%) and Portland cement (10 wt.%) mixtures using sodium silicate (SS) + NaOH as alkaline activators. Molar ratios of $\text{SiO}_2/\text{Al}_2\text{O}_3$ (6.3 to 7.7) and $\text{Na}_2\text{O}/\text{SiO}_2$ (0.07 to 0.16) were used. The cements were prepared at room temperature (25 °C) and characterized by mechanical and physical properties and microstructure. The optimized cement was used for the preparation of novel photoactivated composite materials by incorporating 5 and 10 wt.% TiO_2 (Ti) and ZnO (Z) nanoparticles, and its self-cleaning and bactericidal properties were evaluated by means of the degradation of rhodamine-B (Rh-B) and the growth inhibition of *Klebsiella pneumoniae* and *Pseudomonas aeruginosa* bacteria. The results of this study showed that the 100SS-5Z and 50SS:50G-10Ti cements have an effective photocatalytic activity for Rh-B degradation of 98.4% and 76.4%, respectively, after 24 h. Additionally, the 100SS-5Z and 50SS:50G-10Ti cement pastes and their respective mortars were effective in inhibiting the growth of *Pseudomonas Aeruginosa* and *Klebsiella pneumoniae* bacterial strains, evidenced by the formation of bacterial inhibition halos around the sample discs. Finally, these results are novel, and open the possibility of using constructions and demolition tile waste in high proportions for the elaboration of new rendering mortar with innovative properties.

Keywords: ceramics tile wastes; alkali activation; self-cleaning cement; bactericidal cement



Citation: Bonilla, A.; Villaquirán-Cacedo, M.A.; Mejía de Gutiérrez, R. Novel Alkali-Activated Materials with Photocatalytic and Bactericidal Properties Based on Ceramic Tile Waste. *Coatings* **2022**, *12*, 35. <https://doi.org/10.3390/coatings12010035>

Academic Editors: Inês Flores-Colen, Hideyuki Kanematsu and Anibal C. Maury-Ramirez

Received: 11 November 2021

Accepted: 26 December 2021

Published: 28 December 2021

Publisher's Note: MDPI stays neutral with regard to jurisdictional claims in published maps and institutional affiliations.



Copyright: © 2021 by the authors. Licensee MDPI, Basel, Switzerland. This article is an open access article distributed under the terms and conditions of the Creative Commons Attribution (CC BY) license (<https://creativecommons.org/licenses/by/4.0/>).

1. Introduction

It is known that the widespread use of ordinary Portland cement (OPC) in the construction industry has a high environmental impact. It is estimated that this industry represents approximately 36% of global energy consumption and generates 39% of the emissions of CO_2 during construction activities [1] due to the high temperatures necessary for the production of clinker (approximately 1450 °C) and the burning of fuels. Thus, the search for alternatives for the manufacture of alternative binders that involve partial or total replacement of OPC has become a worldwide trend. [2]. Different alternatives have been proposed, including alkali-activated cements from raw materials rich in aluminosilicates mixed with an alkaline solution composed of silicate and alkali metal hydroxide, where the most commonly used are silicate and sodium hydroxide. Although the cements produced from this process are considered low carbon footprint cements [3–6], the alkaline activator is the component that contributes the most to the environmental impact of alkali-activated materials, especially sodium silicate (SS), which contributes approximately between 47% and 65% of the total equivalent CO_2 emissions of the alkali-activated materials [5,7]. The different raw materials for the manufacture of alkali-activated cements include calcined clays, such as metakaolin [8]; fly ash [9]; blast furnace slag [10–12]; different agricultural byproducts, such as rice husk ash [13] and sugarcane bagasse [14]; and construction and demolition waste [15], such as concrete [16,17] and brick [18–21]. Construction and demolition waste are materials of great interest because of their large volume generated

worldwide and because the levels of use do not reach 30% globally [22]. However, few studies have been reported on the use of waste ceramic (CW) [23,24]. The alkaline activation process involves four main stages. It begins with a process of dissolution of the aluminosilicate sources to create three-dimensional and interconnected polymer networks through polycondensation [25]. The reaction product between the alkaline activator and the aluminosilicate filler material depends on the chemical composition of the precursor. In the case of the alkaline activation of low calcium precursors, such as type F fly ash, and the use of a sodium alkaline activator, an amorphous sodium aluminosilicate hydrate (NASH) gel is obtained as the main reaction product [26].

Several authors recommend implementing thermal curing to promote and accelerate the alkaline activation process, generally at temperatures of approximately 60 °C [27]. As an alternative to thermal curing, it is possible to use OPC in small quantities to decrease the setting time of the pastes at room temperature and to increase the compressive strength of the samples. The authors of [24] used ceramic residue with 15% OPC to obtain a compressive strength of 58.15 MPa after 28 days of curing in pastes. The inclusion of blast furnace slag is also quite common in the production of alkali-activated pastes due to its high CaO content, which promotes the formation of calcium silicate hydrate (CSH) and calcium aluminosilicate hydrate (CASH) gels [28], which can harden at a room temperature of 25 °C. It has been reported that alkali-activated materials have good durability in hostile environments, such as in the presence of chlorides, [29], acids [30], and sulfates [31]. Some research carried out with CW shows that mixing CW with 40% fly ash can obtain a compressive strength of 45.9 MPa and shows a better performance in a sulfuric acid environment [12]. The authors of [32] also demonstrated that it is possible to use ceramic residues together with fly ash for the synthesis of pastes resistant to high temperatures and marine environments, finding that the inclusion of 10% ceramic residues in alkaline activated pastes with 90% fly ash improved the compressive strength after exposure to high temperatures and a simulated marine environment.

Recently, construction materials with photocatalytic properties (cementitious matrix composites with the incorporation of semiconductor nanoparticles such as TiO₂, ZnO, or CuO) have been developed for application on exterior surfaces with the aim of reducing environmental pollution through the generation of “active surfaces” [33–41]. The introduction of nanoparticles allows for the generation of radicals on the surface of the material, which provide self-cleaning properties [8,40–42] and, in some cases, the inhibition of the growth of bacteria, important characteristics in environments where the elimination of these priority biological agents is required, such as health centers and hospital care [43–46]. According to the literature consulted, there is little research on the reuse of CDW [46] in the formulation of alkali-activated cements with active surfaces. In addition, the use of these activated cements using CW and glass wastes in the synthesis of materials for self-cleaning and bactericidal applications has not been documented. This research evaluates the synthesis of alkali-activated cements from white CW and its application in the degradation of organic inks (rhodamine-B (Rh-B)), and studies its bactericidal effect on *Klebsiella pneumoniae* and *Pseudomonas aeruginosa*.

2. Materials and Methods

2.1. Materials

The aluminosilicate precursor for the preparation of materials via alkaline activation, CW, was mechanically conditioned in a jaw mill, followed by a ball mill (Mechanical CAD, Cali, Colombia) for 8 h, until a fine aluminosilicate precursor powder was obtained. Additionally, OPC (cement for general use, UG, according to the Colombian NTC 121 standard) was used in the mixtures to facilitate hardening at room temperature. Commercial SS (produced by *Productos Químicos Panamericanos*[®], Cali, Colombia) F₄₇ was used as an activator, with 12.1 wt.% Na₂O, 31.4 wt.% SiO₂, and 56.5 wt.% H₂O. Sodium hydroxide (NaOH) flakes with a purity of 99.7% were used to prepare the alkaline solution. Clear glass wastes were used to evaluate their potential as an alkaline activator and as a fine

aggregate in the preparation of rendering mortar. ZnO (PanReact AppliChem 131786.1211, Barcelona, Spain) and TiO₂ (Aeroxide TiO₂, P25) particles were used for the preparation of the photocatalytic composites.

2.2. Preparation of Alkali-Activated Materials

To obtain alkali-activated cements, a mixture of 85 wt.% CW with 15 wt.% OPC was used. In the preliminary tests, it was found that it was necessary to incorporate OPC to facilitate the hardening of the material at room temperature. A statistical design (Minitab 18 software) of the response surface methodology (RSM) was proposed to study the variables involved in the alkaline activation of the CW. In the RSM, the molar ratios of Na₂O/SiO₂ and SiO₂/Al₂O₃ of the mixes were evaluated, and the response variable was the compressive strength at 28 days of curing. The proposed experiments are shown in Table 1. The synthesis of the alkali-activated cement consisted of mixing the solids (CW + OPC) with the alkaline solution (SS + NaOH + water) in a Hobart mixer for 5 min until a homogeneous paste was obtained. The mass liquid/solid ratio (L/S) was adjusted to 0.26 in all mixtures. At the end of the mixing time, the paste obtained was poured into cubic molds of 20 mm per side, vibrated to release the trapped air bubbles, and then wrapped with a plastic film to prevent the water from evaporating. The specimens were stored in a curing chamber with ~90% relative humidity for 24 h at a temperature of 25 °C. After this time, the samples were removed from the mold and were stored until reaching the required test age

Table 1. Molar ratios for the synthesis of hybrid cements obtained from the RSM design with Minitab 18 software.

Mixture	Molar Ratio Na ₂ O/SiO ₂	Molar Ratio SiO ₂ /Al ₂ O ₃	Molar Ratio NaOH/ ¹ SiO ₂
M1	0.12	7	2.87
M2	0.08	7.5	0.48
M3	0.12	7	2.87
M4	0.12	7	2.87
M5	0.08	6.5	5.77
M6	0.15	7.5	2.10
M7	0.12	7	2.87
M8	0.12	6.3	32.05
M9	0.07	7	1.10
M10	0.12	7	2.87
M11	0.12	7.7	1.10
M12	0.16	7	4.28
M13	0.15	6.5	12.04

¹ SiO₂ calculated from SS.

For the second stage of the study, the pastes with the best compressive strength results were chosen, and 50% of the SS was replaced by glass, to finally form photoactivated composites such as pastes and mortars (paste/fine glass aggregate ratio of 1:1) with TiO₂ and ZnO incorporated at 5% and 10% by weight. Their photocatalytic activity (through the degradation of Rh-B) and biological activity (through the inhibition of the bacterial growth of *K. pneumoniae* and *P. aeruginosa*) were evaluated. It should be noted that, the electron-positive hole coupling due to the proximity between active sites generates loss of the efficiency of the photocatalytic action, and, accordingly, a low depolluting effectiveness and antimicrobial activity. This vicinity may be a direct consequence of the type and quantity of nano-sized particles, which show a sharp trend to agglomerate reducing the catalyst area, although at the same time they provide a greater number of active sites [45,47]. Therefore, methods to optimize the dosage of nanoparticles and to fully exploit the performance of nanomaterials in cementitious composites are still being studied [43,48]. Thus, the proportion of nanoparticles used in conventional cement must be controlled in order to avoid agglomeration and subsequent loss of their photocatalytic effects, suggesting values of the

order of 5% [49,50]. Nevertheless, in geopolymer cements, the incorporation of nanoparticles in percentages of up to 10 wt.% has shown efficiency in photocatalysis and physical properties by increasing the bulk density and decreasing water absorption [8,51,52].

2.3. Characterization Techniques

The following techniques were used to characterize the raw materials and the alkaline cements obtained:

- The average particle size of the CW precursor was determined using a Mastersizer 2000 laser granulometer (Malvern Instrument, Malvern, UK). The density of the CW raw material was determined by the pycnometer technique, following ASTM standard C127-04. The chemical composition of the CW and glass waste was determined with an Axios mAX sequential wavelength-dispersive X-ray fluorescence (WDXRF) spectrometer (PANalytical, Tollerton, UK) equipped with a rhodium tube and operated with a maximum power of 4.0 kW with SuperQ software version 5.0 L.
- The compressive strengths of the alkali activated materials were obtained according to ASTM C109 using 20 mm cubic specimens. The tests were carried out on an Instron 3369 universal testing machine (Instron, Norwood, MA, USA) at a displacement speed of 1 mm/min. The data reported correspond to the average of the four test specimens.
- The surfaces of the pieces obtained after the mechanical tests were observed with scanning electron microscopy (SEM) using a JEOL JSM-6490LV instrument (JEOL, Tokyo, Japan) with a 20 kV acceleration voltage. The pieces observed had been previously coated with gold, and the observations were made in high vacuum mode (3×10^{-6} torr). An Oxford Instruments Link-Isis X-ray spectrometer (Oxford Instruments, Abingdon, UK) was coupled to the microscope for energy-dispersive spectrometry (EDS).
- X-ray diffraction (XRD) of the CW and pastes was performed using an X'Pert MRD PANalytical (Malvern-PANalytical, Malvern, UK) diffractometer with Cu K α 1 radiation at 20 mA and 40 kV. The samples were scanned at 2θ angles between 5° and 60° , at a step rate of 0.02 and a holding time of 4.0 s per step.
- The physical properties of the pastes as the bulk density, percent absorption, and volume of permeable pores were determined according to ASTM C642, with the modification of leaving the samples submerged in water at 100°C for 3 h instead of the 5 h specified in the standard for OPC-based materials. The data reported correspond to the average of the three test specimens.
- For the degradation of Rh-B, discs 3 cm in diameter and 4 mm in height were prepared from all pastes with 5 and 10 wt.% of TiO₂ particles and ZnO particles. The determination of the photocatalytic activity was evaluated using a method based on that used by [40], performing the immersion of the samples in 10 mL of Rh-B with a concentration of 5 ppm, and using exposure to ultraviolet light for 24 h. UV-A radiation was supplied by two mercury lamps (ELECTROLUX T8 20w/BLB) located inside a black acrylic dome. These lamps emit light at an intensity of $10.3\text{ W}\cdot\text{m}^{-2}$, which was measured with a Delta Ohm HD 2102.2 photoradiometer (Delta Ohm, Caselle, Italy) using the filter for UV-A light with a range of 5 nm. For each measurement, 1 mL aliquot was deposited in 50 mL of distilled water in a Falcon tube for centrifuge, and then a sample was taken and placed into quartz cell of 2 mL. The degradation efficiency after 24 h was monitored at a wavelength of 554 nm using a Shimadzu UV–VIS spectrophotometer (Shimadzu, Columbia, MD, USA), model UV-1800 series A1145450047OCD.
- The biological activity of the materials was evaluated through the inhibition of the bacterial growth [46] of ATCC strains of *K. pneumoniae* (ATCC[®] 13883TM) and *P. aeruginosa* (ATCC[®] 27853TM) acquired from the ATCC cell bank, similarly to method presented by [46,53,54]. The cylindrical samples (4 cm in diameter and 2 mm thick for pastes and 2.6 cm in diameter for mortars) were exposed to ultraviolet light ($\lambda = 360\text{ nm}$) for 24 h in a chamber with a lamp at 10.3 Wm^{-2} intensity prior to the test with bacteria,

similar to [54,55]. The antimicrobial activity test on cement mortars irradiated with the UVA light shortened the inactivation time of the bacteria and, additionally, it was possible to compare them with the action of natural daylight [53–55]. Afterwards, each bacterial inoculum was added to LB agar at 37 °C, and was homogenized and served in Petri dishes; then, the material to be evaluated (paste or mortar) was placed in the center of the box and left in a flow cabinet until gelling. It was incubated for 18 h at 37 °C. After incubation, each plate was examined and visualized for the presence of colonies grown on the surface of the material or the formation of inhibition halos was registered. The culture medium and supplements used were BHI Broth (Becton Dickinson, Franklin Lakes, NJ, USA), Luria Bertani Agar (Becton Dickinson, Franklin Lakes, NJ, USA), saline solution (Corpaul, Medellín, Colombia), and saline phosphate buffer (Bio-Connect, Huissen, The Netherlands). A Sensi-disc control of gentamicin was used (6 mm in diameter and 2 mm thick).

3. Results and Discussion

3.1. Raw Materials

Figure 1 shows the appearance of CW before and after being mechanically proceeded. Initially, the CWs were collected and dried at room temperature (25 °C) for 24 h, and were mechanically processed by hammer milling followed by ball milling (2 h). The chemical composition of the raw materials is shown in Table 2. The CW is composed mainly of SiO₂ and Al₂O₃, at 89.9%, and the density of the CW was of 2600 kg/m³. The SiO₂/Al₂O₃ molar ratio for the CW is 6.2. The average particle size D [3,4] for the CW is 45.4 μm, with d(0.1) 2.7 μm, d(0.5) 23.3 μm, and d(0.9) 122.2 μm.

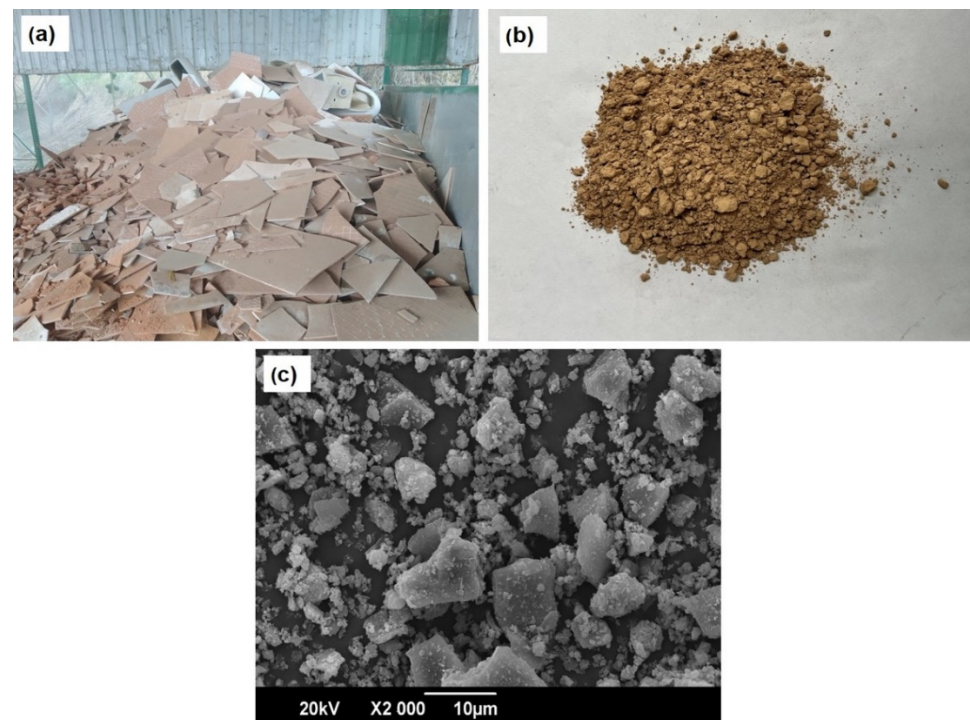


Figure 1. Ceramic tile wastes (CW): (a) before crushing, (b) after crushing, and grinding (c) SEM image.

Table 2. Chemical composition for raw materials.

Compounds	CW	OPC	Glass Waste
	(wt.%)		
SiO ₂	70.6	17.9	72.27
Al ₂ O ₃	19.3	3.90	1.49
Fe ₂ O ₃	4.3	4.80	0.62
Na ₂ O	-	0.20	13.37
K ₂ O	2.4	0.30	0.51
CaO	2.0	62.30	11.15
MgO	0.8	1.80	0.26
LOI, 1000 °C	0.6	4.10	1.46

The particles used for the experiments were ZnO (PanReact AppliChem 131786.1211, Barcelona, Spain) and TiO₂ (Aeroxide[®] P25, Essen, Germany), and both particles were smaller than 1 µm. Zinc oxide is a semiconductor with a high thermal conductivity, high exciting binding energy (60 m eV), and wide band gap, i.e., 3.2–3.4 eV, and the size of particles ranges from 16 to 140 nm [56]. Aeroxide[®] (Essen, Germany) P25 is a flame made multiphasic TiO₂ nanoparticles containing anatase and rutile; the size of primary nanoparticles ranges from 10 to 50 nm, largely distributed from 15 to 20 nm [57,58]. OPC type UG (Cemex[®], Cali, Colombia) was used in order to obtain alkali activated cements at a room temperature of 25 °C. Glass wastes were crushed to be used as (i) precursor powder (density of 2411 kg/m³) to replace SS in alkaline activation and to be (ii) used as fine aggregates in the preparation of mortars. The alkaline activator was generated from a mixture of SS PQP F47 with 12.1% Na₂O and 31.4% SiO₂ with a sodium hydroxide solution (NaOH, 99.7%).

3.2. Characterization of the CW-OPC Hybrid Pastes

The compressive strength was determined at different ages (7, 28, and 90 days of curing), and the results are shown in Figure 2a. For a better understanding of the results, a contour graph of the statistical analysis (Figure 2b) shows the influence of the design variables on the compressive strength after 28 days of curing. The darkest green areas correspond to the best compressive strengths, and optimization of the results occur in the mixtures M9, which obtained a compressive strength of 40.1 ± 0.84 MPa, and M11, with 42.04 ± 1.07 MPa, at age of 28 days. There is a dependence between the synthesis variables SiO₂/Al₂O₃ (Si/Al) and Na₂O/SiO₂ (Na/Si) and the compressive strength; for a Na/Si ratio greater than 0.09, the strength values fall below 25 MPa. An increase in the Na/Si ratio is correlated with a decrease in the amount of SS in the alkaline activator, while a low Na/Si ratio is achieved with a greater amount of SS and lower amounts of NaOH. It is known that an increase in the alkalinity of the paste can affect the polymerization process [59]. The authors of [60] state that increasing the Na/Si ratio increases the percentage of open pores by almost 65% in alkali-activated fly ash samples and consequently reduces the compressive strength. In this study, it is observed that an increase in the Si/Al ratio with a low Na/Si ratio increased the compressive strength of the pastes, especially when the Si/Al ratio is greater than 7. As the content of Al in the pastes comes from the CW and OPC, the Si/Al ratio is modified with the alkaline activator, so an increase in the Si/Al ratio also corresponds to an increase in the amount of SS in the mixture. Several authors agree that excess sodium content in the mixture generates efflorescence on the surface of the material, which can affect the compressive strength [13,61,62].

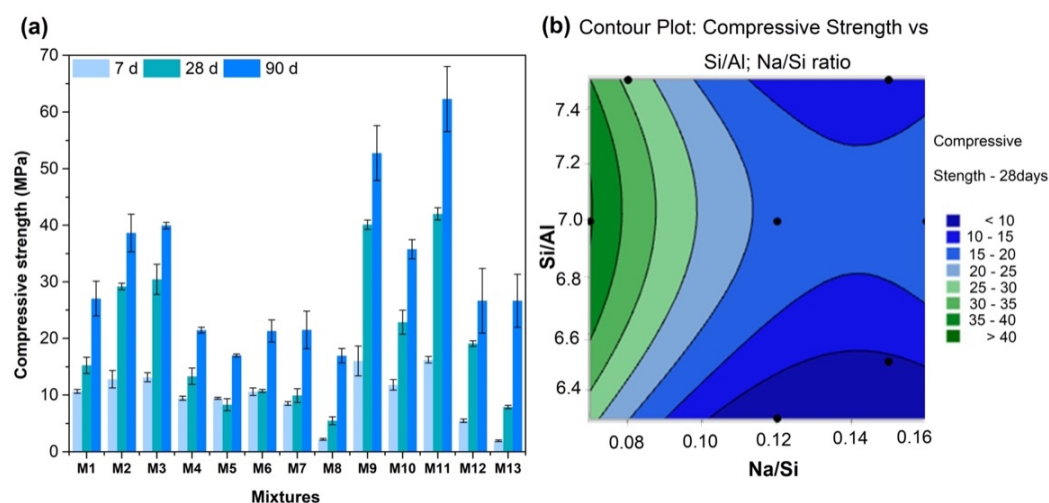


Figure 2. (a) Compressive strength at ages of 7, 28, and 90 days for cements 85%CW–15%OPC. (b) Contour statistic plots.

From the mixtures shown in Table 1, pastes with a high NaOH/SiO₂ ratio (reactive and soluble SiO₂ from silicate), such as M1 (2.87), M4 (2.87), M5 (5.77), M6 (2.10), M7 (2.87), M8 (32.05), M12 (4.28), and M13 (12.04), have lower compressive strength at all evaluated ages, while pastes with a low NaOH/SiO₂ ratio, such as M2 (0.48), M9 (1.10), and M11 (1.10), show the highest strengths. In the case of the M5, M8, and M13 pastes, it is evident that the contribution of the soluble SiO₂ content that comes from the SS, which is essential in the development of compressive strength [63,64], is very low. Mixtures M5 and M8, despite having Na₂O contents similar to those of M9 and M11, have a SiO₂/Al₂O₃ molar ratio similar to that of the raw material (6.2), so the incorporation of SS is low in these pastes, thus hindering the formation of gels that provide mechanical strength to the material. Similar results have been reported by [19].

In Figure 2a, for early ages, M9 and M11 have a similar behavior to compression. However, after 90 days of curing, the M11 paste presented a compressive strength above 60 MPa, higher than M9. This may be because the dosage in M11 contributes a higher content of both SS, that is, soluble silica, to the mixture, which can promote the formation of hydrated aluminosilicate gels at later ages.

The mineralogical composition of the CW and hybrid pastes M9 and M11 was analyzed by XRD, and the results obtained are presented in Figure 3. The SiO₂ of the raw material CW is mainly in the crystalline state in a quartz structure ($2\theta = 22.3^\circ, 28.7^\circ, 49.7^\circ, \text{ and } 54.5^\circ$), and it persists in pastes M9 and M11 after alkaline activation. Authors such as [18,23,65] corroborate that the alkaline activation processes do not dissolve the quartz present in the raw material. The formation of new peaks for M9 and M11 are identifiable at angles of $21.95^\circ, 43.15^\circ, \text{ and } 48.53^\circ$, corresponding to the formation of alkali carbonates [19,66,67]. New peaks are also identified at 29.39° and 47.53° , corresponding to CSH produced from the hydration of the OPC used in the mixtures. The presence of hybrid sodium calcium aluminosilicate hydrate (N-CASH) gel is also identified and corroborates the results found by other authors [19,67–69]. These small peaks are explained by the presence of 15% OPC in the mixture, which contributes Ca²⁺ ions, promoting the formation of these gels in the microstructure, and are corroborated by the SEM-EDS assay presented below (Figure 5a,b). The authors of [70] found that the alkaline activation of precursors with high calcium contents can yield CASH, similar to the hydrated calcium silicate gel CSH produced in the exclusive hydration of OPC pastes. The XRD and compressive strength results show that the performance obtained for the pastes depends on the degree of polymerization and the formation of gels; thus, low ratios of NaOH/Na₂SiO₃ promote a greater degree of polymerization and the formation of gel types N-CASH and CSH, that is, when higher contents of soluble silicate SS are incorporated into the mixture [19,71].

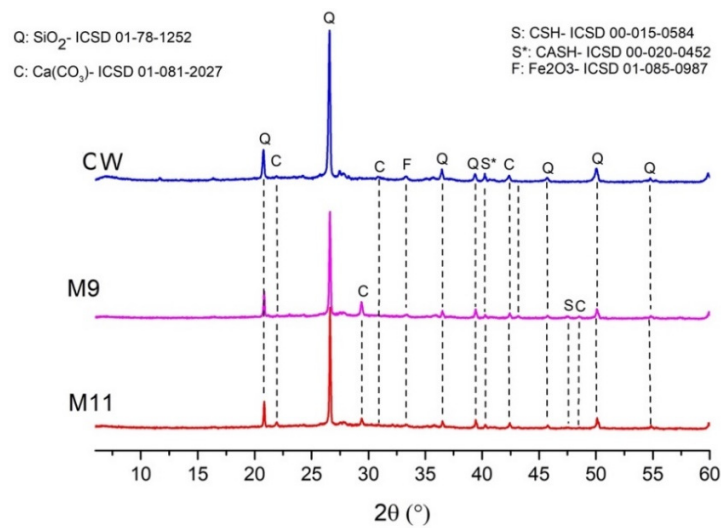


Figure 3. XRD for M9 and M11 mixtures at the age of 90 days compared to the CW raw material.

To evaluate glass (G) as a precursor in M9 and M11, 50 wt.% SS was replaced by G and, in turn, the OPC content was lowered to 10 wt.% to further reduce the carbon footprint of the mixtures. For these pastes, it was necessary to adjust the L/S ratio to 0.36 in order to obtain a paste with adequate workability that could be mixed and emptied into the molds. The results for the compressive strength of the hybrid pastes M9 and M11 with a replacement of 50% SS by G are shown in Figure 4. It was found that the replacement of SS by G reduced the compressive strength of the pastes at the ages of 7 and 28 days of curing. The loss of strength at age 28 days reached 97% for M9 and 73.57% for M11 with the replacement of SS by G. This behavior is attributed to the fact that the incorporation of G as a substitute for SS initially provides less amorphous SiO_2 compared to SS [60]. The authors of [69] suggest that the optimal conditions for obtaining SS from glass waste involve 6 h of agitation at a temperature of 85°C to achieve a solution comparable to commercial SS. In this investigation, glass was added directly to an alkaline solution of NaOH [9.6 M], allowed to stand for 20 min, and was subsequently emptied and mixed with the CW + OPC solids, so that the glass was dissolved to obtain SiO_2 reagent similar to SS; this is an extra reaction that must occur before starting the alkaline activation process and providing the percentage of Na_2O and SiO_2 of the design [72]. Due to the process conditions used in this research (25°C and short mixing time), the kinetics of the geopolymerization reaction when using G are affected by its low dissolution, and consequently the formation of N-CASH and CSH gels is reduced.

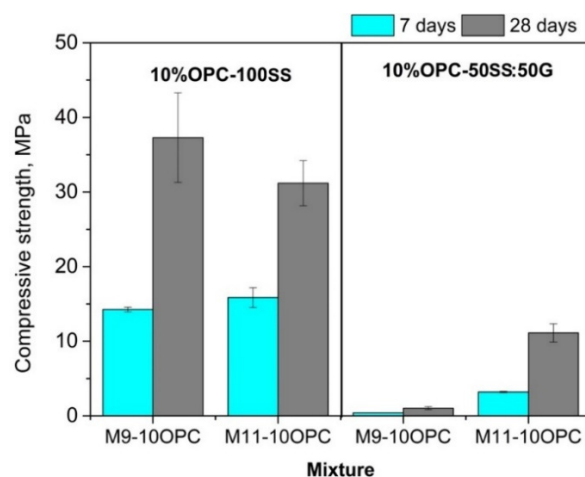


Figure 4. Compressive strength for hybrid pastes CW-OPC with different contents of SS.

The SEM-EDS results of pastes M9 and M11 (Figure 5a,b) with 100% SS show a smoother and more homogeneous surface for M11, as well as a lower presence of micro-cracks, caused by shrinkage processes by drying and evaporation during the hardening stage [73,74] compared to the M9 paste, which indicates the formation of a denser and more homogeneous M11 matrix. The SEM images of the pastes with replacement of SS by G (Figure 5c,d) reveal a very heterogeneous surface, with extensive cracking and little cohesiveness. These results demonstrate the low polymerization capacity of fine glass under the conditions studied, which is reflected in its poor mechanical performance. Table 3 shows the EDS results of pastes with 50% SS:50% G, which confirm a large amount of Si and O in the system due to the presence of unreacted glass particles.

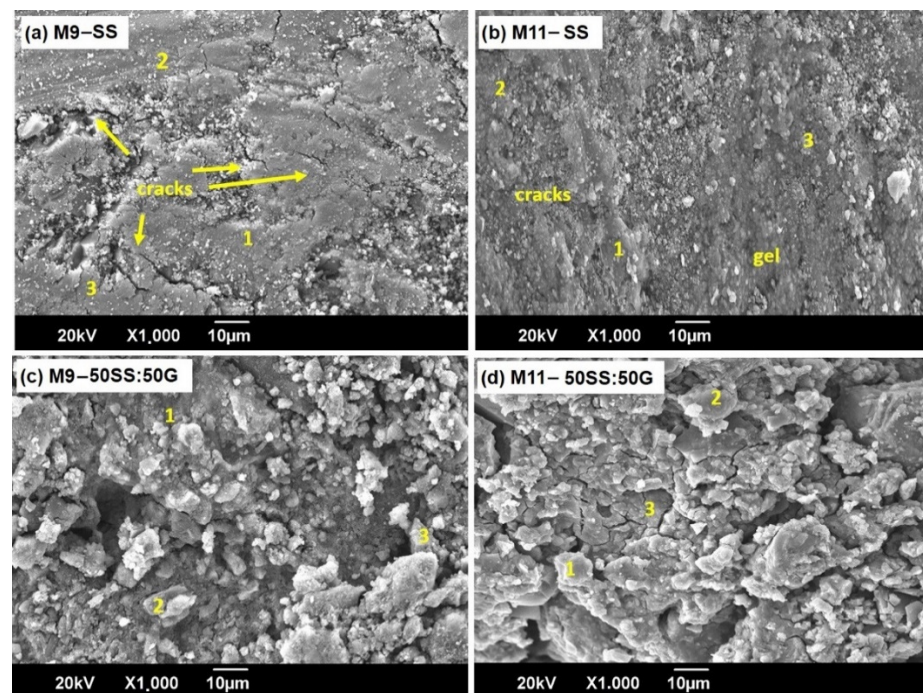


Figure 5. SEM images for pastes: (a) M9-100SS, (b) M11-100SS, (c) M9-50SS:50G, (d) M11-50SS:50G.

In Table 3, the EDS spectra are shown for points 1, 2, and 3 identified in Figure 5. It is possible to identify CASH, N-CASH, and portlandite gels, carbonated species, and Fe from the unreacted raw material. The initial reactions in hybrid systems with an OPC content indicate hydration of the cement as the first reaction, generating CSH and portlandite ($\text{Ca}(\text{OH})_2$), which is subsequently carbonated [64]. The polycondensation of geopolymers is favored by the presence of calcium, which comes mainly from the OPC in the mixture [19] and reacts with the system ($\text{Na}_2\text{O}-\text{CaO}-\text{Al}_2\text{O}_3-\text{SiO}_2-\text{H}_2\text{O}$) to form hybrid N-CASH gels [68]. The formation of the hybrid gels that coexist in various proportions is due to the dissolution and condensation reaction of the tetrahedra of $[\text{SiO}_4]^{4-}$ and $[\text{AlO}_2]^-$ from the CW, which reacts over time and is incorporated in the structure of the CSH [67], which is reflected by the increase in mechanical strength at older ages (Figure 2). Sodium and calcium ions are located in the interstices of the amorphous structure formed by polysialates, and balance the negative charges in the structure [64,75].

Table 3. EDS for M9 y M11 with 100SS and 50SS:50G: Composition (wt.%) and Interpretation.

Paste	Spectrum	C	O	Na	Al	Si	K	Ca	Fe	Ca/Si Ratio	Interpretation
M9-100SS	1	25.59	28.41	2.59	11.86	25.59	1.31	1.72	2.93	0.06	N(C)–A–S–H, CaCO ₃ ,
	2	27.86	39.25	2.86	9.90	14.76	0.69	1.58	3.09	0.10	N(C)–A–S–H, CaCO ₃ ,
	3	25.80	31.60	3.78	6.97	24.06	1.23	4.70	1.86	0.19	(N),C–A–S–H, CaCO ₃
M11-100SS	1	41.33	24.24	2.62	4.33	20.03	1.67	5.78	-	0.29	(N),C–A–S–H, CaCO ₃
	2	34.40	19.74	2.35	9.59	29.04	-	4.88	-	0.17	(N),C–A–S–H, CaCO ₃
	3	-	25.50	-	4.14	20.57	-	49.78	-	2.42	C–(A)–S–H, portlandite
M9-50SS:50G	1	11.62	45.68	10.36	1.67	25.47	-	5.21	-	0.20	N ₁ (C)–A–S–H, Na ₂ CO ₃
	2	14.27	32.81	6.91	2.92	19.33	1.38	19.90	2.49	1.02	(N),C–A–S–H, (Ca,Na)CO ₃
	3	16.74	44.93	10.85	3.84	18.94	1.31	2.32	1.06	0.12	N ₁ (C)–A–S–H, Na ₂ CO ₃
M11-50SS:50G	1	15.95	45.22	1.44	2.19	34.41	-	0.79	-	0.03	N ₁ (C)–A–S–H, Na ₂ CO ₃
	2	21.58	40.22	4.73	6.38	23.21	0.87	1.50	1.51	0.07	N ₁ (C)–A–S–H, Na ₂ CO ₃
	3	12.34	48.56	10.32	4.79	17.25	1.06	3.75	1.93	0.22	N ₁ (C)–A–S–H, Ca,Na ₂ CO ₃

OPC promotes the formation of CSH, with a lower Ca/Si ratio than the CSH that is normally formed by OPC hydration [76], and due to the contents of Al and Na, the precipitation of N-CASH is possible as the main hydration product according to the Ca/Si ratio and the contents of Na and Al obtained [67]. The Ca/Si ratios are higher in M11, indicating a higher inclusion of Ca for this sample, which generates the highest mechanical strengths because the silica of the silicate reacts with the calcium ions and generates the CSH gel [26]. On the other hand, the residual alkali that does not react to form gels or that is trapped in the pores by its excess reacts with the carbon of the atmosphere to form alkali carbonates, which has been previously observed by other authors [67,77]. The EDS results confirm the previously shown XRD results for pastes M9 and M11.

In Table 4, the values of the physical properties of pastes M9 and M11 with 100% SS are shown. Although the density found in M9 was similar to the density of M11, the porosity and absorption were lower for M11 by 17.85% and 25.40%, respectively. The lower porosity of M11 allowed the paste to support higher loads, and, therefore, its strength was greater. The density values found for M9 and M11 were similar to those reported by [61] (1220 and 1540 kg/m³) by activating fly ash with SS. The authors of [60] reported a percentage of open pores between 25% and 40% for activated pastes based on Italian fly ash, and between 23% and 43% for the ash of an Australian origin. They were also similar to those reported by [67], who reported porosity percentages between 28% and 31% for alkali-activated construction demolition waste pastes.

Table 4. Physical properties for pastes M9 y M11 with 100% SS.

Mixture	Dry Density, kg/m ³	Apparent Density, kg/m ³	Porosity, %	Water Absorption, %
M9	1820 ± 10	2520 ± 10	28 ± 0.38	15.3 ± 0.2
M11	1870 ± 20	2430 ± 10	23 ± 0.36	12.2 ± 0.2

Based on these results, the M9 paste was discarded, and henceforth, the M11 paste activated with silicate and glass (M11-50SS:50G) and M11 100% commercial silicate (M11-SS) were used to develop mortars using paste/recycled fine aggregate ratios of 1:1. Additionally, the mechanical strengths of the mortars made with M11-SS and the natural aggregate of river sand (MRef) were evaluated. The compressive strengths at 28 days of curing were 25.21, 11.57, and 9.08 MPa, for the MRef, M11-SS, and M11-50SS:50G mortars, respectively. As expected, the natural aggregate provides greater compressive strength than the recycled glass aggregate. However, it is noteworthy that the workability of the mixture in the fresh state is improved with the incorporation of the recycled aggregate, as the glass is less porous and has a smoother surface than for river sand.

SEM images of the mortar with different SS contents are shown in Figure 6. Figure 6a,b corresponds to mortar with 100SS, and Figure 6c,d to 50SS mortar. It is evident that the interface between the matrix and the aggregate is of a low quality (Figure 6a,d), as extensive microcracks through the surface and great porosity were observed. This explains why the

charge transfer between the matrix and the glass particles was poor; mortar with glass, with its smooth surface and fragile nature, have a weakened interfacial zone, which has been identified by other authors such as [78,79] by replacing sand with glass as an aggregate in OPC-based mortar. In Figure 6a, it can be seen that the morphology of the aggregate (G), which is angular and has a smooth surface appearance, makes it difficult for the paste to adhere to the particle. The natural aggregate in MRef (Figure 6e) has a less angular morphology and is better covered by the paste. Thus, the interface zone between the paste sand was denser due to the greater roughness presented by the natural aggregate [78], which is reflected in an increase of 23% in the compressive strength in the MRef mortar.

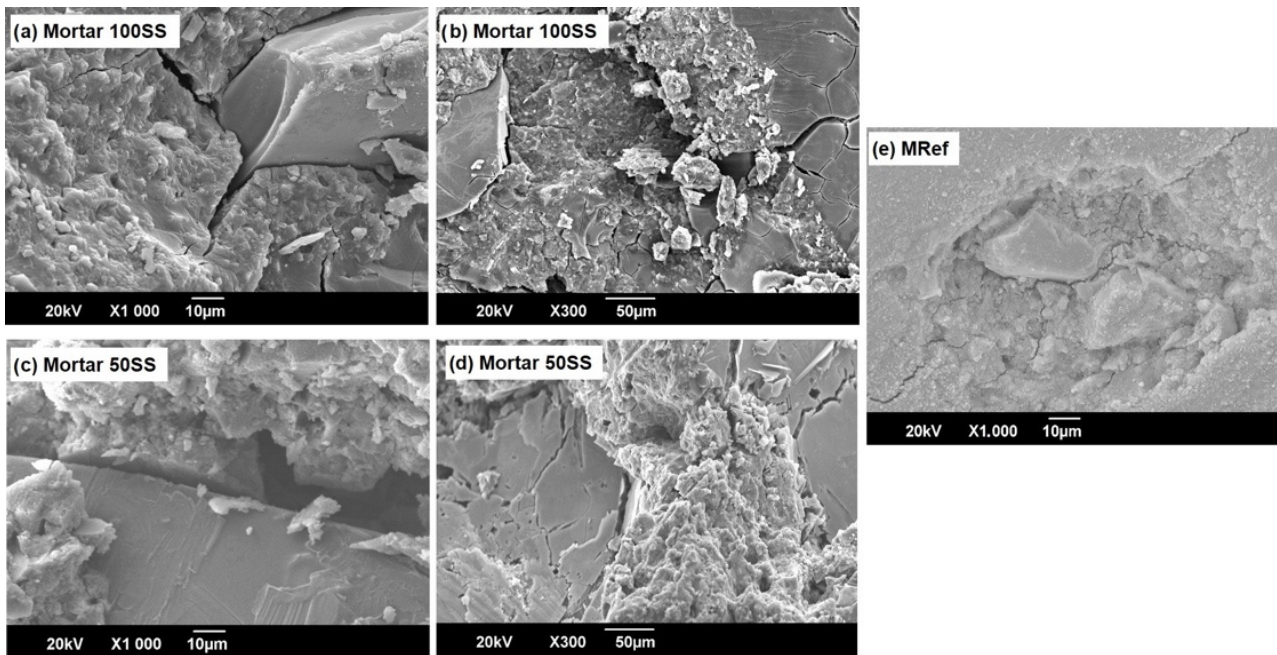


Figure 6. SEM images of mortar based on M11 paste with different SS content using G as a fine aggregate (a–d) and (e) mortar made with M11-100SS and natural aggregate (river sand).

A comparison of the type of activator (100SS, 50SS:50G) using glass as a fine aggregate, showed a strength loss of 21.5% for 50SS:50G compared to the mortar that uses the 100SS matrix. In mortar, the replacement of SS by G generated a more porous microstructure with greater cracking (Figure 6c,d). An increase in micropores when using G was previously observed by [80]. It was also possible to observe a large formation of microcracks around the fine aggregate and to transverse to it, which can be attributed to volumetric contraction and poor adhesion, creating weak interfacial transition zones [79,81]. In general, the fine aggregate (G) did not react significantly with the matrix to create a continuous medium of homogeneous aluminosilicate gels.

3.3. Effect of TiO_2 and ZnO Particles in Mechanical and Photocatalytic Properties

In the M11-SS and 50SS:50G paste, TiO_2 and ZnO particles were incorporated in percentages of 5 and 10 wt.%, with the objective of developing a photocatalytic composite and evaluating the self-cleaning properties. The incorporation of photocatalytic particles reduced the compressive strength, as shown in Figure 7, regardless of the type of binder used (M11-SS or M11-50SS:50G). In the paste with a 50SS:50G silicate source, the strength was between 3.5 and 8.0 MPa, and in the paste with M11-SS, it was between 26–28 MPa. The incorporation of 10%- TiO_2 reduced the compressive strength by 48.33% for the binder with 50SS:50G and 14.11% for the binder with M11-SS. In the case of the incorporation of 10%- ZnO particles, the strength reduction was 15.48% in the 50SS:50G binder and 30.9% in the binder with M11-SS. This behavior can be attributed to a nonhomogeneous

distribution of the nanoparticles in the binder (Figure 9), which causes an agglomeration of the nanoparticles, reduces the binder capability of the matrix, concentrating stress, so cracks can propagate more easily, creating weak interfaces in the structure. Additionally, with the incorporation of particles as replacements and not as additions, the cementing phase was reduced, which contributes to less formation of gels. However, all the mixtures that exceeded the minimum compressive strength required by the UNE-EN 998-1.2018 standard are classified as materials that could be used as rendering mortars in categories CS III (3.5–7.5 MPa) and CS IV (≥ 6.5 MPa). Additionally, the incorporation of photocatalytic particles tends to increase the density of the material (Table 5), because the particles have densities greater than that of the CW starting material, 5.68 g/cm^3 for ZnO and 3.5 g/cm^3 for TiO_2 . Guzmán-Aponte et al. [8] incorporated different amounts of TiO_2 , finding that the density of the composites varied according to the water content of the mixture; however, for mixtures with an L/S ratio of 0.45, an increase in the content of TiO_2 increased the density of the composites.

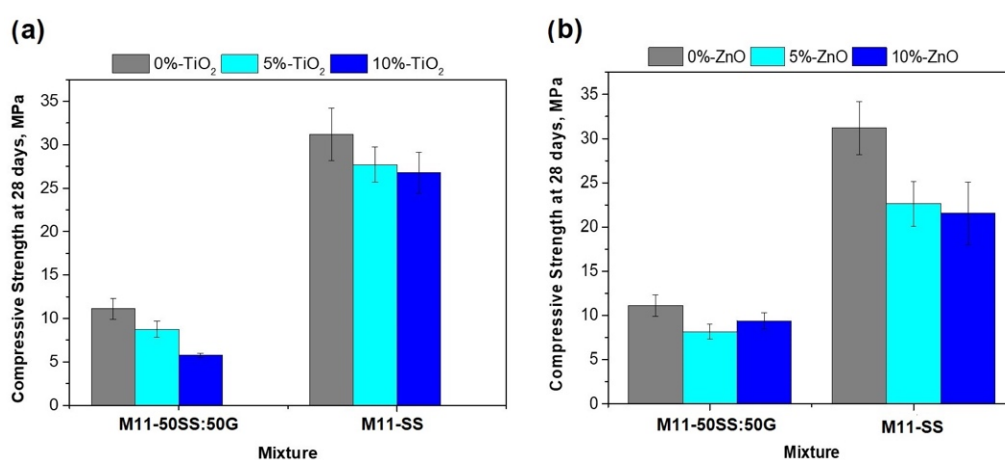


Figure 7. Compressive strength for pastes with incorporation of (a) TiO_2 and (b) ZnO particles.

Table 5. Density of mixtures with incorporation of TiO_2 and ZnO particles.

Mixtures	Density, kg/m^3				
	0%	5%- TiO_2	10%- TiO_2	5%-ZnO	10%-ZnO
M11-SS	1870 ± 20	1880 ± 10	1900 ± 10	1920 ± 10	1970 ± 10
M11-50SS:50G	-	1990 ± 10	2040 ± 20	2040 ± 30	2040 ± 20

The results of UV–VIS spectrometry in terms of the self-cleaning properties of the composite materials are shown in Figure 8, and the values of total degradation of Rh-B after 24 h are shown in Table 6. The mixtures with 100% commercial silicate and 5% ZnO (SS-5Z) present a greater degradation of the ink, reaching 98%. This result is attributed to the fact that there is a good distribution of ZnO particles on the surface of the discs, making the surface of the sample more smooth, as can be observed in the SEM images in Figure 9. For the case of the incorporation of TiO_2 , the mixture is viscous, which makes it difficult to homogenize the mixture; therefore, the particles could tend to agglomerate inside the paste, and made the surface heterogeneous, as observed in Figure 9a,b, causing fewer particles to be exposed on the surface; similar results have been found by [82].

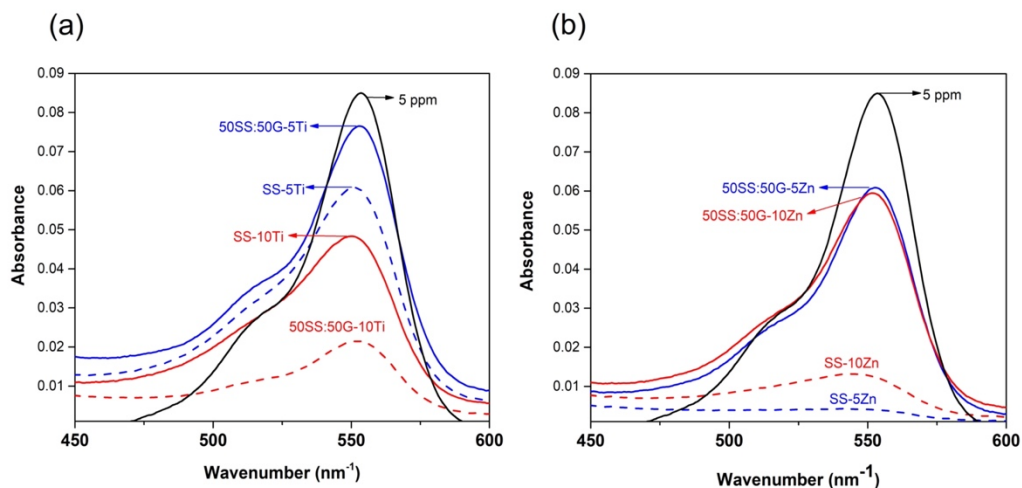


Figure 8. UV – VIS spectrum for different mixtures after 24 h of exposure to RhB with incorporations of (a) TiO₂ and (b) ZnO particles.

Table 6. Percentage of degradation of Rh-B (evaluated at 554 nm) for different mixtures.

Mixture	C/Co after 24 h	Degradation of RhB, %
SS-5Ti	3.4	32,4%
SS-10Ti	2.8	44.5%
50SS:50G-5Ti	4.1	17.0%
50SS:50G-10Ti	1.2	76.4%
SS-5Z	0.1	98.4%
SS-10Z	0.4	91.8%
50SS:50G-5Z	2.0	61.0%
50SS:50G-10Zn	1.9	62.1%

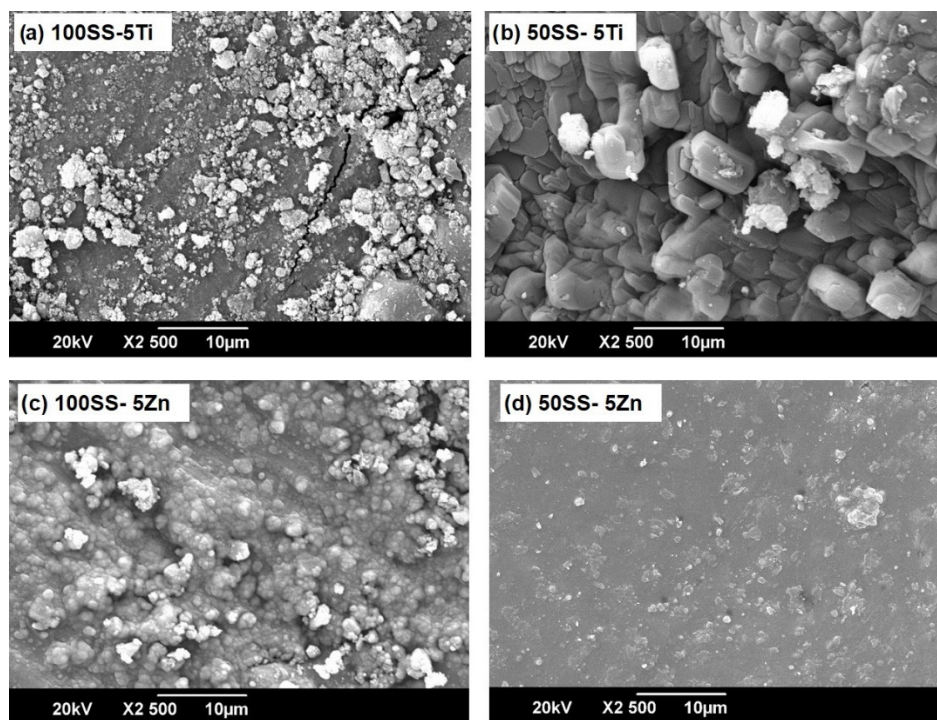


Figure 9. SEM images of composites with (a,b) 5% of TiO₂ and (c,d) 5% of ZnO.

According to Hasmaliza et al. [45] and Loh et al [54], the particle size of TiO₂ influences the contact angle when it is applied on tile surfaces, which is affected by the appearance and photocatalytic test of the glazed agglomeration of TiO₂ particles. In the case of micro-TiO₂, it offered a good dispersion and greater surface area for adsorption and reaction with large molecules such as Rhodamine B [54]. The photocatalytic activity in these materials is due to the incorporation of semiconductor particles capable of interacting with the light in their environment and promoting the passage of electrons from the valence layer of the matter to the conduction bands [83]. This process generates radicals that in turn can interact with organic agents through oxidation–reduction reactions, generating the degradation of these substances [84]. Speciale et al. [85] found that the TiO₂ agglomeration together with the electron–hole recombination in the case of an excess of photocatalyst will put a cap on the final admissible concentration of TiO₂.

Hasmaliza et al. [45] and Loh et al. [54] observed that the number of colonies of *E. coli* was lower with incorporations of nano-TiO₂ than micro-TiO₂, suggesting that TiO₂ segregation plays an important role in the determinations of the photocatalytic activity. Additionally, as stated by Sikora et al. [53], porous structures, which have a larger surface area, are beneficial for the adsorption process, and a high number of pores together with a high total surface area can be favorable for the internal dispersion of pollutants and bacteria removal; nevertheless, the incorporation of nanoparticles decreases the water absorption and densifies the microstructure. According to Wang et al. [86], the contact angle of the surfaces of cement-TiO₂ increases from 15° for the cement control to 66° to 90° for cement with TiO₂ particles, and the angle depends on the type of size of TiO₂ particles with hydrophobic surfaces; similar results of super-hydrophilicity have been found with geopolymer-TiO₂ composites [87]. Additionally, the incorporation of nanoparticles increases the densification of mortars (see Table 5), because TiO₂ mainly acts as a filler to densify the binder [87], for which the photocatalytic effect is assumed to be due to the incorporation of TiO₂ and ZnO and not for the high porosity of mortar.

Likewise, studies of the zeta potential show that nano-TiO₂ requires longer times for the electrostatic stabilization of the particles [47]; therefore, its catalytic effect is poorer and delayed. Thus, it could be expected that the ZnO particles require less time for their electrostatic stabilization, therefore explaining their effective dispersion in the developed material. Additionally, different research on the zeta potential of TiO₂ and ZnO particles at different pH [88,89] have shown that in alkaline pH, the zeta potential of the ZnO particles is more electropositive compared to the zeta potential of the TiO₂ particles, which indicates a better dispersion ability of ZnO in developed geopolymers.

A comparison of these results with those of the UNI 11259:2008 standard for the determination of the photocatalytic activity, which requires a degradation equal to or greater than 50% after 24 h, shows that the pastes containing 5% and 10% ZnO comply with this requirement, while only the 50SS:50G-10Ti paste achieves a degradation greater than 50% (Table 6). Similar results were observed by other authors [40,41], who incorporated ZnO and TiO₂ particles in geopolymer pastes and obtained photocatalytic materials for applications such as exterior construction materials.

3.4. Biological Activity with Bacteria

Based on the photocatalytic assays, the pastes that presented the best performance were 100SS-5Zn and 50SS:50G-10Ti and, for this reason, the biological activity by means of the inhibition of the growth of ATCC strains *K. pneumoniae* and *P. aeruginosa* in the pastes and their respective mortar with recycled fine aggregate (G) was evaluated. Images corresponding to the inhibition halos obtained in cultures of *K. pneumoniae* and *P. aeruginosa* with the evaluated composites and control samples used are shown in Figures 10 and 11, and the results of the inhibition assay are presented in Table 7. Chen et al. [90] confirmed that the photocatalytic activity of mortar is improved when waste glass is incorporated as an aggregate in cement materials, due to the light transmittance property of waste glass, which plays a vital role in the enhancement of the photocatalytic reactions. The light could

be carried to a greater depth, activating the TiO_2 on the surface as well within the surface layer.

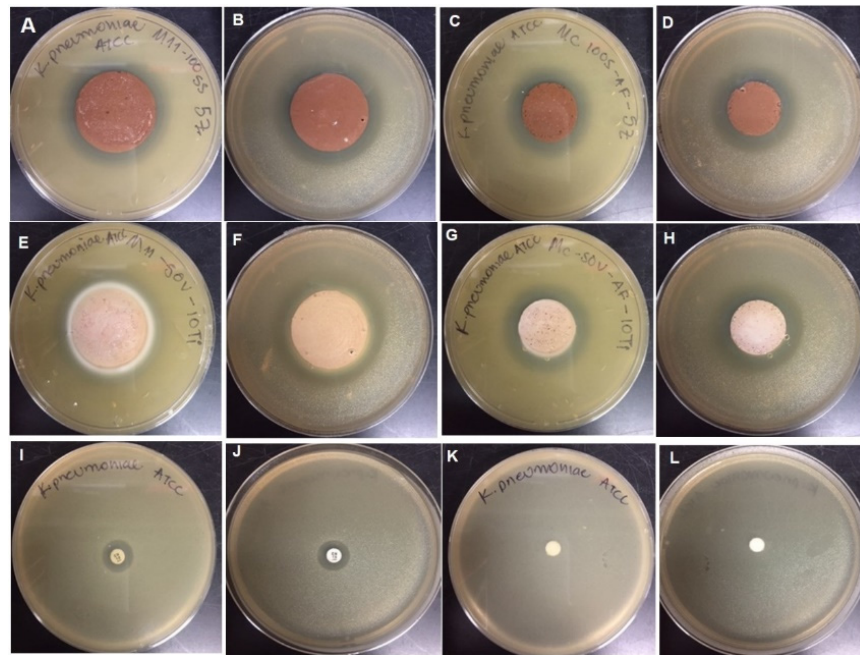


Figure 10. Images corresponding to the agar of *K. pneumoniae* for different mixtures and the control. Front and rear views are presented, respectively. (A,B) paste 100SS-5Z, (C,D) mortar 100SS-AF-5Z-G, (E,F) paste 50SS:50G-10Ti, (G,H) mortar 50SS:50G-AF-10Ti-G, (I,J) Sensi-disc control of gentamicin, and (K,L) Sensi-disc control with no inhibition.

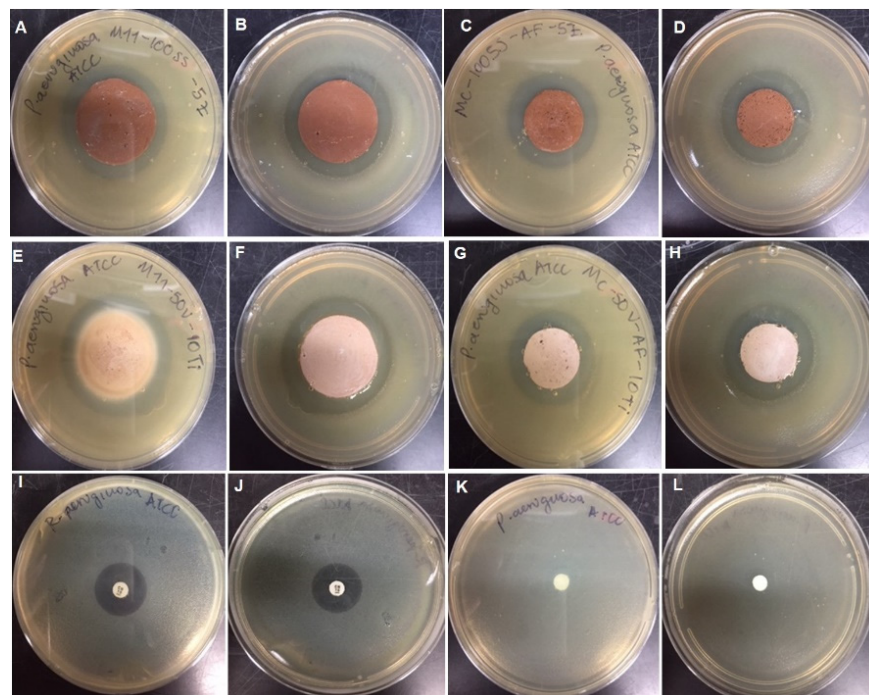


Figure 11. Images corresponding to the culture of *P. aeruginosa* for different mixtures and the control. Front and rear views are presented, respectively. (A,B) Paste 100SS-5Z, (C,D) mortar 100SS-5Z-G, (E,F) paste 50SS:50G-10Ti, (G,H) mortar 50SS:50G-10Ti-G, (I,J) Sensi-disc control of gentamicin, and (K,L) Sensi-disc control with no inhibition.

Table 7. Inhibition halos obtained in the culture of the ATCC strains of *K. pneumoniae* and *P. aeruginosa* with the evaluated materials and controls.

Type	Mixture	Formation of Bacterial Inhibition Halos	
		<i>K. pneumoniae</i> ATCC	<i>P. aeruginosa</i> ATCC
Mortar	50SS:50G-10Ti-G	Yes	Yes
	100SS-5Z-G	Yes	Yes
Paste	100SS-5Z	Yes	Yes
	50SS:50G-10Ti	Yes	Yes
Control	Sensidisc Gentamicin	Yes	Yes
	Sensidisc whithout antibiotic	No	No

It was found that all the evaluated materials inhibited the growth of the evaluated strains, forming bacterial inhibition halos (Figures 10 and 11). The inhibition of bacterial growth is related to the formation of reactive oxygen species (ROS) [91] as a product of the interaction of the photons incident on the surface of the material and the nanoparticles of ZnO and TiO₂ in both the paste and the mortar. Through this mechanism, the material can interact with the cell membranes, ribosomes, or DNA, or simply interfere in the transport of electrons during the oxidation of nicotinamide adenine dinucleotide in bacteria, intervening in the biological mechanisms of bacteria and, ultimately, annihilating them [43,84].

4. Conclusions

The preparation of cement-based composites from the alkaline activation of white CW is a technically viable alternative to produce binders with photocatalytic and bactericidal properties. The results of this study allow for the following conclusions to be drawn:

- The contribution of amorphous and soluble silica from SS is an essential component to achieve compressive strengths in pastes above 10 MPa. A high sodium content in the mixtures reduces the viscosity of the pastes and results in carbonation reactions with the environment, which can generate efflorescence due to carbonated products on the surface of the samples. The formation of the CASH gel and the hybrid N-CASH gel was evidenced by the CW-OPC mixture. The optimal molar ratio values for the preparation of pastes with strengths of 40 MPa at 28 days were 7.7 for SiO₂/Al₂O₃ and 0.12 for Na₂O/SiO₂.
- In the evaluation of the capacity of alternative silicate formation, the replacement of SS by 50% glass was not beneficial due to the poor dissolution of the glass at room temperature and under the alkaline conditions studied. Additionally, the incorporation of glass as a fine aggregate decreased the compressive strengths. The values obtained were 25.21, 11.57, and 9.08 MPa at 28 days of curing for the MRef mortar (made with river sand), M11-SS mortar, and M11-50SS:50G mortar using G as a fine aggregate, respectively. The loss of strength was attributed to the formation of a weakened aggregate–paste transition zone with a high porosity and the formation of microcracks around the glass aggregate.
- The 100SS-5Z and 50G:50SS-10Ti pastes showed an effective photocatalytic activity for Rh-B degradation, with percentages of Rh-B degradation of 98.4% and 76.4%, respectively, after 24 h, but problems of mixing and poor dispersion of the nanoparticles were observed and could be the main technological challenge.
- The 100SS-5Z and 50G:50SS-10Ti pastes, together with their respective mortars, were effective at inhibiting the growth of *P. aeruginosa* and *K. pneumoniae* strains, evidenced by the formation of bacterial inhibition halos around the sample discs.
- These results demonstrated the possibility of using ceramic tile waste in high proportions for the elaboration of new rendering mortar with innovative properties.

Author Contributions: Conceptualization, R.M.d.G. and M.A.V.-C.; methodology and investigation M.A.V.-C. and A.B.; formal analysis, M.A.V.-C. and A.B.; resources, R.M.d.G. and M.A.V.-C.; writing—original draft preparation, M.A.V.-C. and A.B.; writing—review and editing, M.A.V.-C.; final revision, R.M.d.G.; project administration, M.A.V.-C. All authors have read and agreed to the published version of the manuscript.

Funding: This research was funded by UNIVERSIDAD DEL VALLE for financial projects VRI- Grant Nos. C.I 21025 and C.I 21147.

Institutional Review Board Statement: Not applicable.

Informed Consent Statement: Not applicable.

Data Availability Statement: Not applicable.

Conflicts of Interest: The authors declare no conflict of interest.

References

- World Green Building Council. Global Status Report 2017 | World Green Building Council. 2017. Available online: <https://www.worldgbc.org/news-media/global-status-report-2017> (accessed on 11 September 2021).
- Purushotham, K.B.; Chandra Mohan, D.V.; Janardhan Yadav, M.; Naga Ratna Giri, P.S. Comparative studies on LC3 based concrete with OPC & PPC based concretes. *Mater. Today Proc.* **2021**, *43*, 2368–2372. [\[CrossRef\]](#)
- Batuecas, E.; Ramón-Álvarez, I.; Sánchez-Delgado, S.; Torres-Carrasco, M. Carbon footprint and water use of alkali-activated and hybrid cement mortars. *J. Clean. Prod.* **2021**, *319*, 128653. [\[CrossRef\]](#)
- Garcés, J.I.T.; Dollente, I.J.; Beltran, A.B.; Tan, R.R.; Promentilla, M.A.B. Life cycle assessment of self-healing geopolymers. *Clean. Eng. Technol.* **2021**, *4*, 100147. [\[CrossRef\]](#)
- Robayo, R.A.; Mejía-Arcila, J.; Mejía de Gutiérrez, R.; Martínez, E. Life cycle assessment (LCA) of an alkali-activated binary concrete based on natural volcanic pozzolan: A comparative analysis to OPC concrete. *Constr. Build. Mater.* **2018**, *176*, 103–111. [\[CrossRef\]](#)
- Salas, D.A.; Ramirez, A.D.; Ulloa, N.; Baykara, H.; Boero, A.J. Life cycle assessment of geopolymer concrete. *Constr. Build. Mater.* **2018**, *190*, 170–177. [\[CrossRef\]](#)
- Villaquirán-Cacedo, M.A.; Mejía de Gutiérrez, R. Synthesis of ceramic materials from ecofriendly geopolymer precursors. *Mater. Lett.* **2018**, *230*, 300–304. [\[CrossRef\]](#)
- Guzmán-Aponte, L.A.; Mejía de Gutiérrez, R.; Maury-Ramírez, A. Metakaolin-Based geopolymer added TiO₂ particles: Physico-mechanical characteristics. *Coatings* **2017**, *7*, 233. [\[CrossRef\]](#)
- Dehghani, A.; Aslani, F.; Ghaebi Panah, N. Effects of initial SiO₂/Al₂O₃ molar ratio and slag on fly ash-based ambient cured geopolymer properties. *Constr. Build. Mater.* **2021**, *293*, 123527. [\[CrossRef\]](#)
- Tayeh, B.A.; Zeyad, A.M.; Agwa, I.S.; Amin, M. Effect of elevated temperatures on mechanical properties of lightweight geopolymer concrete. *Case Stud. Constr. Mater.* **2021**, *15*, e00673. [\[CrossRef\]](#)
- Khan, M.N.N.; Kuri, J.C.; Sarker, P.K. Effect of waste glass powder as a partial precursor in ambient cured alkali activated fly ash and fly ash-GGBFS mortars. *J. Build. Eng.* **2020**, *34*, 101934. [\[CrossRef\]](#)
- Joudah, Z.H.; Huseien, G.F.; Samadi, M.; Shukor Lim, N.H.A. Sustainability evaluation of alkali-activated mortars incorporating industrial wastes. *Mater. Today Proc.* **2021**, *45*, 1971–1977. [\[CrossRef\]](#)
- Villaquirán-Cacedo, M.A. Studying different silica sources for preparation of alternative waterglass used in preparation of binary geopolymer binders from metakaolin/boiler slag. *Constr. Build. Mater.* **2019**, *227*, 116621. [\[CrossRef\]](#)
- Athira, V.S.; Charitha, V.; Athira, G.; Bahurudeen, A. Agro-waste ash based alkali-activated binder: Cleaner production of zero cement concrete for construction. *J. Clean. Prod.* **2021**, *286*, 125429. [\[CrossRef\]](#)
- Tefa, L.; Bassani, M.; Coppola, B.; Palmero, P. Strength development and environmental assessment of alkali-activated construction and demolition waste fines as stabilizer for recycled road materials. *Constr. Build. Mater.* **2021**, *289*, 123017. [\[CrossRef\]](#)
- Ouda, A.S. A preliminary investigation on gamma-ray attenuation of alkali-activated concrete waste based-geopolymer modified with pozzolane-fly ash. *Prog. Nucl. Energy* **2021**, *134*, 103681. [\[CrossRef\]](#)
- Das, S.K.; Shrivastava, S. Influence of molarity and alkali mixture ratio on ambient temperature cured waste cement concrete based geopolymer mortar. *Constr. Build. Mater.* **2021**, *301*, 124380. [\[CrossRef\]](#)
- Hwang, C.L.; Dantie Yehualaw, M.; Vo, D.H.; Huynh, T.P. Development of high-strength alkali-activated pastes containing high volumes of waste brick and ceramic powders. *Constr. Build. Mater.* **2019**, *218*, 519–529. [\[CrossRef\]](#)
- Robayo, R.A.; Mulford, A.; Munera, J.; Mejía de Gutiérrez, R. Alternative cements based on alkali-activated red clay brick waste. *Constr. Build. Mater.* **2016**, *128*, 163–169. [\[CrossRef\]](#)
- Sedira, N.; Castro-Gomes, J.; Magrinho, M. Red clay brick and tungsten mining waste-based alkali-activated binder: Microstructural and mechanical properties. *Constr. Build. Mater.* **2018**, *190*, 1034–1048. [\[CrossRef\]](#)
- Rakhimova, N.R.; Rakhimov, R.Z. Alkali-activated cements and mortars based on blast furnace slag and red clay brick waste. *Mater. Des.* **2015**, *85*, 324–331. [\[CrossRef\]](#)

22. Robayo-Salazar, R.A.; Matthey Centeno, P.E.; Silva Urrego, Y.F.; Burgos Galindo, D.M.; Delvasto, S. Construction and demolition wastes: Analysis of its management and reuse in Cali. *Rev. Tecnura* **2015**, *19*, 157–170.
23. Huseien, G.F.; Sam, A.R.M.; Shah, K.W.; Mirza, J. Effects of ceramic tile powder waste on properties of self-compacted alkali-activated concrete. *Constr. Build. Mater.* **2020**, *236*, 117574. [[CrossRef](#)]
24. Murillo, L.M.; Delvasto, S.; Gordillo, M. A study of a hybrid binder based on alkali-activated ceramic tile wastes and Portland cement. In *Sustainable and Nonconventional Construction Materials using Inorganic Bonded Fiber Composites*; Savastano, H., Fiorelli, J., Dos Santos, S.F., Eds.; Elsevier: Amsterdam, The Netherlands, 2017; pp. 291–311.
25. Davidovits, J. Properties of geopolymer cements. In *First International Conference on Alkaline Cements and Concrete*; Kiev State Technical University: Kyiv, Ukraine, 1994; pp. 131–149. Available online: http://www.geopolymer.org/fichiers_pdf/KIEV.pdf (accessed on 3 September 2021).
26. Torres-Carrasco, M.; Puertas, F. Alkaline activation of different aluminosilicates as an alternative to Portland cement: Alkali activated cements or geopolymers. *Rev. Ing. Constr.* **2017**, *32*, 5–12. [[CrossRef](#)]
27. Ibrahim, M.; Maslehuiddin, M. An overview of factors influencing the properties of alkali-activated binders. *J. Clean. Prod.* **2021**, *286*, 124972. [[CrossRef](#)]
28. Xiao, R.; Zhang, Y.; Jiang, X.; Polaczyk, P.; Ma, Y.; Huang, B. Alkali-activated slag supplemented with waste glass powder: Laboratory characterization, thermodynamic modelling and sustainability analysis. *J. Clean. Prod.* **2021**, *286*, 125554. [[CrossRef](#)]
29. Amorim Júnior, N.S.; Andrade Neto, J.S.; Santana, H.A.; Cilla, M.S.; Ribeiro, D.V. Durability and service life analysis of metakaolin-based geopolymer concretes with respect to chloride penetration using chloride migration test and corrosion potential. *Constr. Build. Mater.* **2021**, *287*, 122970. [[CrossRef](#)]
30. Saloni Parveen, Y.Y.; Pham Jatin, T.M.; Kumar, J. Sustainable alkali activated concrete with fly ash and waste marble aggregates: Strength and durability studies. *Constr. Build. Mater.* **2021**, *283*, 122795. [[CrossRef](#)]
31. Siddique, S.; Jang, J.G. Acid and sulfate resistance of seawater based alkali activated fly ash: A sustainable and durable approach. *Constr. Build. Mater.* **2021**, *281*, 122601. [[CrossRef](#)]
32. Ouda, A.S.; Gharieb, M. Behavior of alkali-activated pozzocrete-fly ash paste modified with ceramic tile waste against elevated temperatures and seawater attacks. *Constr. Build. Mater.* **2021**, *285*, 122866. [[CrossRef](#)]
33. Maury, A.; De Belie, N. State of the art of TiO₂ containing cementitious materials: Self-cleaning properties. *Mater. Construcción* **2010**, *60*, 33–50. [[CrossRef](#)]
34. Haider, A.J.; Al-Anbari, R.H.; Kadhim, G.R.; Salame, C.T. Exploring potential environmental applications of TiO₂ nanoparticles. *Energy Procedia* **2017**, *119*, 332–345. [[CrossRef](#)]
35. Mohd Adnan, M.A.; Muhd Julkapli, N.; Amir, M.N.I.; Maamor, A. Effect on different TiO₂ photocatalyst supports on photodecolorization of synthetic dyes: A review. *Int. J. Environ. Sci. Technol.* **2019**, *16*, 547–566. [[CrossRef](#)]
36. Baheiraei, N.; Moztarzadeh, F.; Hedayati, M. Preparation and antibacterial activity of Ag/SiO₂ thin film on glazed ceramic tiles by sol-gel method. *Ceram. Int.* **2012**, *38*, 2921–2925. [[CrossRef](#)]
37. Drugă, B.; Ukrainczyk, N.; Weise, K.; Koenders, E.; Lackner, S. Interaction between wastewater microorganisms and geopolymer or cementitious materials: Biofilm characterization and deterioration characteristics of mortars. *Int. Biodeterior. Biodegrad.* **2018**, *134*, 58–67. [[CrossRef](#)]
38. Abo-El-Enein, S.A.; El-Hosiny, F.I.; El-Gamal, S.M.A.; Amin, M.S.; Ramadan, M. Gamma radiation shielding, fire resistance and physicochemical characteristics of Portland cement pastes modified with synthesized Fe₂O₃ and ZnO nanoparticles. *Constr. Build. Mater.* **2018**, *173*, 687–706. [[CrossRef](#)]
39. Guo, M.Z.; Maury-Ramirez, A.; Poon, C.S. Photocatalytic activities of titanium dioxide incorporated architectural mortars: Effects of weathering and activation light. *Build. Environ.* **2015**, *94*, 395–402. [[CrossRef](#)]
40. Zailan, S.N.; Mahmed, N.; Abdullah, M.M.A. Photocatalytic activity of ZnO-doped geopolymer paste. *IOP Conf. Ser. Mater. Sci. Eng.* **2020**, *864*, 012038. [[CrossRef](#)]
41. Zailan, S.N.; Mahmed, N.M.; Abdullah, M.M.A. Photocatalytic behaviour of TiO₂-geopolymer paste under Sunlight photocatalytic behaviour of TiO₂-geopolymer paste under sunlight. *IOP Conf. Ser. Mater. Sci. Eng.* **2020**, *957*, 012006. [[CrossRef](#)]
42. Abdel-Gawwad, H.A.; Mohamed, S.A.; Mohammed, M.S. Recycling of slag and lead-bearing sludge in the cleaner production of alkali activated cement with high performance and microbial resistivity. *J. Clean. Prod.* **2019**, *220*, 568–580. [[CrossRef](#)]
43. Sikora, P.; Augustyniak, A.; Cendrowski, K.; Nawrotek, P.; Mijowska, E. Antimicrobial activity of Al₂O₃, CuO, Fe₃O₄, and ZnO nanoparticles in scope of their further application in cement-based building materials. *Nanomaterials* **2018**, *8*, 212. [[CrossRef](#)] [[PubMed](#)]
44. Dahiya, M.S.; Tomer, V.K.; Duhan, S. Bioactive glass/glass ceramics for dental applications. In *Applications of Nanocomposite Materials in Dentistry*; Asiri, A.M., Inamuddin, A.M., Eds.; Elsevier: Amsterdam, The Netherlands, 2018; pp. 1–25.
45. Hasmaliza, M.; Foo, H.S.; Mohd, K. Anatase as antibacterial material in ceramic tiles. *Procedia Chem.* **2016**, *19*, 828–834. [[CrossRef](#)]
46. Mejía de Gutiérrez, R.; Villaquirán-Caicedo, M.A.; Ramírez-Benavides, S.; Astudillo, M.; Mejía, D. Evaluation of the antibacterial activity of a geopolymer mortar based on metakaolin supplemented with TiO₂ and CuO particles using glass waste as fine aggregate. *Coatings* **2020**, *10*, 157. [[CrossRef](#)]
47. González-Sánchez, J.F.; Taşçı, B.; Fernández, J.M.; Navarro-Blasco, I.; Alvarez, J.I. Improvement of the depolluting and self-cleaning abilities of air lime mortars with dispersing admixtures. *J. Clean. Prod.* **2021**, *292*, 126069. [[CrossRef](#)]

48. Kawashima, S.; Seo, J.W.; Corr, D.; Hersam, M.C.; Shah, S.P. Dispersion of CaCO₃ nanoparticles by sonication and surfactant treatment for application in fly ash-cement systems. *Mater. Struct. Constr.* **2014**, *47*, 1011–1023. [[CrossRef](#)]
49. Nurul Reffa Azyan, N.; Norkhairunnisa, M.; Tay, C.H.; Azmah Hanim, M.A. Techniques on dispersion of nanoparticles in polymer matrices: A review. *Pertanika J. Sci. Technol.* **2017**, *25*, 1073–1084.
50. Maury-Ramirez, A.; de Belle, N. Application of TiO₂ photocatalysis to cementitious materials for self-cleaning purposes. In *Application of Titanium Dioxide Photocatalysis to Construction Materials*; Ohama, Y., van Gemert, D., Eds.; Springer: Dordrecht, The Netherlands, 2011; pp. 11–15.
51. Mejía de Gutiérrez, R.; Villaquirán-Cacedo, M.A.; Guzmán-Aponte, L. Alkali-activated metakaolin mortars using glass waste as fine aggregate: Mechanical and photocatalytic properties. *Constr. Build. Mater.* **2020**, *235*, 117510. [[CrossRef](#)]
52. Syamsidar, D.; Nurfadilla; Subaer. The properties of nano TiO₂-geopolymer composite as a material for functional surface application. *MATEC Web Conf.* **2017**, *97*, 01013. [[CrossRef](#)]
53. Sikora, P.; Augustyniak, A.; Cendrowski, K.; Horszczaruk, E.; Rucinska, T.; Nawrotek, P.; Mijowska, E. Characterization of mechanical and bactericidal properties of cement mortars containing waste glass aggregate and nanomaterials. *Materials* **2016**, *9*, 701. [[CrossRef](#)]
54. Loh, K.; Gaylarde, C.C.; Shirakawa, M.A. Photocatalytic activity of ZnO and TiO₂ nanoparticles for use in cement mixes. *Constr. Build. Mater.* **2018**, *167*, 853–859. [[CrossRef](#)]
55. Yemmireddy, V.K.; Hung, Y.C. Effect of binder on the physical stability and bactericidal property of titanium dioxide (TiO₂) nanocoatings on food contact surfaces. *Food Control* **2015**, *57*, 82–88. [[CrossRef](#)]
56. Noman, M.T.; Amor, N.; Petru, M.; Mahmood, A.; Kejzlar, P. Photocatalytic behaviour of zinc oxide nanostructures on surface activation of polymeric fibres. *Polymers* **2021**, *13*, 1227. [[CrossRef](#)]
57. Jiang, X.; Manawan, M.; Feng, T.; Zhao, T.; Zhou, G.; Kong, F.; Wang, Q.; Dai, S.; Pan, J.H. Anatase and rutile in evonik aerioxide P25: Heterojunctioned or individual nanoparticles? *Catal. Today* **2016**, *300*, 12–17. [[CrossRef](#)]
58. Zhang, T.; Li, K.; Pan, J.H. Annealing temperature-dependent electrochemical properties of Aeroxide P25 TiO₂ nanoparticles as anode material for lithium storage. *Prog. Nat. Sci. Mater. Int.* **2019**, *29*, 679–684. [[CrossRef](#)]
59. Huang, G.; Yang, H.; Sun, Y.; Lu, Z.; Zhang, X.; Zuo, L.; Feng, Y.; Qian, R.; Qi, Y.; Ji, Y.; et al. Influence of NaOH content on the alkali conversion mechanism in MSWI bottom ash alkali-activated mortars. *Constr. Build. Mater.* **2020**, *248*, 118582. [[CrossRef](#)]
60. Bignozzi, M.C.; Manzi, S.; Natali, M.E.; Rickard, W.D.; Van Riessen, A. Room temperature alkali activation of fly ash: The effect of Na₂O/SiO₂ ratio. *Constr. Build. Mater.* **2014**, *69*, 262–270. [[CrossRef](#)]
61. Bocullo, V.; Vitola, L.; Vaiciukyniene, D.; Kantautas, A.; Bajare, D. The influence of the SiO₂/Na₂O ratio on the low calcium alkali activated binder based on fly ash. *Mater. Chem. Phys.* **2021**, *258*, 123846. [[CrossRef](#)]
62. Cheng, H.; Lin, K.L.; Cui, R.; Hwang, C.L.; Chang, Y.M.; Cheng, T. The effects of SiO₂/Na₂O molar ratio on the characteristics of alkali-activated waste catalyst–metakaolin based geopolymers. *Constr. Build. Mater.* **2015**, *95*, 710–720. [[CrossRef](#)]
63. Carvalho, R.; Silva, R.V.; de Brito, J.; Pereira, M.F.C. Alkali activation of bottom ash from municipal solid waste incineration: Optimization of NaOH- and Na₂SiO₃-based activators. *J. Clean. Prod.* **2021**, *291*, 125930. [[CrossRef](#)]
64. Sata, V.; Chindaprasirt, P. Use of construction and demolition waste (CDW) for alkali-activated or geopolymer concrete. In *Advances in Construction and Demolition Waste Recycling*; Pacheco-Torgal, F., Ding, Y., Koutamanis, A., Eds.; Elsevier: Amsterdam, The Netherlands, 2020; pp. 385–403.
65. Shah, K.W.; Huseien, G.F. Bond strength performance of ceramic, fly ash and GBFS ternary wastes combined alkali-activated mortars exposed to aggressive environments. *Constr. Build. Mater.* **2020**, *251*, 119088. [[CrossRef](#)]
66. Hanjitsuwan, S.; Injorhor, B.; Phoo-ngernkham, T.; Damrongwiriyanupap, N.; Li, L.-Y.; Sukontasukkul, P.; Chindaprasirt, P. Drying shrinkage, strength and microstructure of alkali-activated high-calcium fly ash using FGD-gypsum and dolomite as expansive additive. *Cem. Concr. Compos.* **2020**, *114*, 103760. [[CrossRef](#)]
67. Villaquirán-Cacedo, M.A.; Mejía de Gutiérrez, R. Comparison of different activators for alkaline activation of construction and demolition wastes. *Constr. Build. Mater.* **2021**, *281*, 122599. [[CrossRef](#)]
68. Kamath, M.; Prashant, S.; Kumar, M. Micro-characterisation of alkali activated paste with fly ash-GGBS-metakaolin binder system with ambient setting characteristics. *Constr. Build. Mater.* **2021**, *277*, 122323. [[CrossRef](#)]
69. Torres-Carrasco, M.; Puertas, F. Waste glass as a precursor in alkaline activation: Chemical process and hydration products. *Constr. Build. Mater.* **2017**, *139*, 342–354. [[CrossRef](#)]
70. Garcia-Lodeiro, I.; Palomo, A.; Fernández-Jiménez, A.; MacPhee, D.E. Compatibility studies between N-A-S-H and C-A-S-H gels. Study in the ternary diagram Na₂O-CaO-Al₂O₃-SiO₂-H₂O. *Cem. Concr. Res.* **2011**, *41*, 923–931. [[CrossRef](#)]
71. Cristelo, N.; Fernández-Jiménez, A.; Vieira, C.; Miranda, T.; Palomo, A. Stabilisation of construction and demolition waste with a high fines content using alkali activated fly ash. *Constr. Build. Mater.* **2018**, *170*, 26–39. [[CrossRef](#)]
72. Tchakouté, H.K.; Rüscher, C.H.; Kong, S.; Kamseu, E.; Leonelli, C. Geopolymer binders from metakaolin using sodium waterglass from waste glass and rice husk ash as alternative activators: A comparative study. *Constr. Build. Mater.* **2016**, *114*, 276–289. [[CrossRef](#)]
73. Panizza, M.; Natali, M.; Garbin, E.; Ducman, V.; Tamburini, S. Optimization and mechanical-physical characterization of geopolymers with Construction and Demolition Waste (CDW) aggregates for construction products. *Constr. Build. Mater.* **2020**, *264*, 120158. [[CrossRef](#)]

74. Kuenzel, C.; Vandeperre, L.J.; Donatello, S.; Boccaccini, A.R.; Cheeseman, C. Ambient temperature drying shrinkage and cracking in metakaolin-based geopolymers. *J. Am. Ceram. Soc.* **2012**, *95*, 3270–3277. [[CrossRef](#)]
75. Mendes, B.C.; Pedroti, L.G.; Vieira, C.M.; Marvilla, M.; Azevedo, A.R.G.; de Carvalho, J.M.F.; Ribeiro, J.C.L. Application of eco-friendly alternative activators in alkali-activated materials: A review. *J. Build. Eng.* **2021**, *35*, 102010. [[CrossRef](#)]
76. Yip, C.K.; Van Deventer, J.S.J. Microanalysis of calcium silicate hydrate gel formed within a geopolymeric binder. *J. Mater. Sci.* **2003**, *38*, 3851–3860. [[CrossRef](#)]
77. Aouan, B.; Alehyen, S.; Fadil, M.; El Alouani, M.; Khabbazi, A.; Atbir, A.; Taibi, M. Compressive strength optimization of metakaolin-based geopolymer by central composite design. *Chem. Data Collect.* **2021**, *31*, 100636. [[CrossRef](#)]
78. Ling, T.C.; Poon, C.S. Properties of architectural mortar prepared with recycled glass with different particle sizes. *Mater. Des.* **2011**, *32*, 2675–2684. [[CrossRef](#)]
79. Arias-Erazo, J.; Villaquirán-Cacedo, M.A.; Goyes, C.E. Ecological light transmitting concrete made from glass waste and acrylic sheets. *Constr. Build. Mater.* **2021**, *304*, 124644. [[CrossRef](#)]
80. Nahi, S.; Leklou, N.; Khelidj, A.; Oudjit, M.N.; Zenati, A. Properties of cement pastes and mortars containing recycled green glass powder. *Constr. Build. Mater.* **2020**, *262*, 120875. [[CrossRef](#)]
81. Sasui, S.; Kim, G.; Nam, J.; van Riessen, A.; Hadzima-Nyarko, M. Effects of waste glass as a sand replacement on the strength and durability of fly ash/GGBS based alkali activated mortar. *Ceram. Int.* **2021**, *47*, 21175–21196. [[CrossRef](#)]
82. Strini, A.; Roviello, G.; Ricciotti, L.; Ferone, C.; Messina, F.; Schiavi, L.; Corsaro, D.; Cioffi, R. TiO₂-based photocatalytic geopolymers for nitric oxide degradation. *Materials* **2016**, *9*, 513. [[CrossRef](#)]
83. Macphee, D.E.; Folli, A. Photocatalytic concretes—The interface between photocatalysis and cement chemistry. *Cem. Concr. Res.* **2016**, *85*, 48–54. [[CrossRef](#)]
84. Wang, L.; Hu, C.; Shao, L. The antimicrobial activity of nanoparticles: Present situation and prospects for the future. *Int. J. Nanomed.* **2017**, *12*, 1227–1249. [[CrossRef](#)]
85. Speziale, A.; González-Sánchez, B.; Tasci, B.; Pastor, A.; Sánchez, L.; Fernández-Acevedo, C.; Oroz-Mateoc Lurederra Tech, T.; Salazar, C.; Navarro-Blasco, I.; Fernández, J.M.; et al. Development of multifunctional coatings for protecting stones and lime mortars of the architectural heritage. *Int. J. Archit. Herit.* **2020**, *14*, 1008–1029. [[CrossRef](#)]
86. Wang, D.; Hou, P.; Zhang, L.; Yang, P.; Cheng, X. Photocatalytic and hydrophobic activity of cement-based materials from benzyl-terminated-TiO₂ spheres with core-shell structures. *Constr. Build. Mater.* **2017**, *148*, 176–183. [[CrossRef](#)]
87. Sanalkumar, K.; Yang, E. Self-cleaning performance of nano-TiO₂ modified metakaolin-based geopolymers. *Cem. Concr. Compos.* **2020**, *115*, 103847. [[CrossRef](#)]
88. Liao, D.L.; Wu, G.S.; Liao, B.Q. Zeta potential of shape-controlled TiO₂ nanoparticles with surfactants. *Colloids Surf. Physicochem. Eng. Asp.* **2009**, *348*, 270–275. [[CrossRef](#)]
89. Marsalek, R. Particle size and zeta potential of ZnO. *APCBEE Procedia* **2014**, *9*, 13–17. [[CrossRef](#)]
90. Chen, J.; Shi-cong, K.; Poon, C. Photocatalytic cement-based materials: Comparison of nitrogen oxides and toluene removal potentials and evaluation of self-cleaning performance. *Build. Environ.* **2011**, *46*, 1827–1833. [[CrossRef](#)]
91. Dizaj, S.M.; Lotfipour, F.; Barzegar-Jalali, M.M.; Zarrintan, H.; Adibkia, K. Antimicrobial activity of the metals and metal oxide nanoparticles. *Mater. Sci. Eng. C* **2014**, *44*, 278–284. [[CrossRef](#)] [[PubMed](#)]